

Numerical modeling of plunging jets of brine: Mass transport and implications for desalination plant outfalls

Matthew T. Flavin ^{a,b,1}, Jenifer Fernandes ^{c,1}, Rawan AlQabandi ^c, Eric Adams ^d, Jongyoon Han ^e, Bader Al-Anzi ^{c,*}

^a Electronics Division, Draper Laboratory, 555 Technology Square, Cambridge, MA 02139, USA

^b Department of Electrical Engineering & Computer Science, Massachusetts Institute of Technology, Cambridge, MA 02139, USA

^c Environment Technology Management, College of Life Sciences, Kuwait University, P.O. Box 5969, Safat 13060, Kuwait

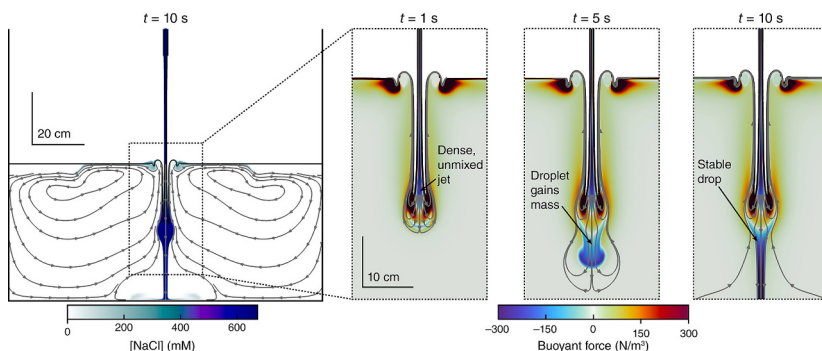
^d Department of Civil and Environmental Engineering, Massachusetts Institute of Technology, Cambridge, MA 02139, USA

^e Department of Electrical Engineering and Computer Science, Massachusetts Institute of Technology, Cambridge, MA 02139, USA

HIGHLIGHTS

- We applied the finite element method to study brine transport in a plunging jet.
- Our model reproduced gravity-driven impingement of brine on the floor of a pool.
- We identified two regimes of brine transport with different mixing performances.
- By enhancing air mass transfer, we could promote a favorable transport regime.
- Effective jet mixing will help prevent deterioration of marine ecosystems.

GRAPHICAL ABSTRACT



ARTICLE INFO

Keywords:

Volume of fluid
Finite element method
Attractor
Euler–Lagrange
Cahn–Hilliard

ABSTRACT

Plunging jets are used in many environmental and industrial applications to enhance mixing and mass transfer rates. One of the current challenges in applying plunging jet reactors for brine dispersal from desalination plants is that the density of brine causes the jet to drop straight to the seafloor. This hypoxic fluid disperses slowly and elicits a toxic effect on the local marine ecosystem. To provide new insights and improvements, we have developed a numerical model that considers the co-transport of brine in a two-phase air–fluid system. In our model, Navier–Stokes describes the transport of fluid, and Nernst–Planck describes the transport of dissolved brine. One of the key observations we made is that brine convection is characterized by competition between the positive buoyancy of air–fluid mixtures and the negative buoyancy of brine–fluid mixtures. Depending on the jet flow rate, the brine would either (1) ascend radially from the plume or (2) drop straight downwards. In our experiments, we demonstrate the same behaviors. Ultimately, it may be possible to reduce the destructive effects of high-density brine impinging on the seafloor by optimizing the jet to promote air entrainment, thus maintaining the system in its radial mixing regime.

* Corresponding author.

E-mail address: bader.alanzi@ku.edu.kw (B. Al-Anzi).

¹ These authors contributed equally to this work

Abbreviations

PLJR	plunging liquid jet reactor
VOF	volume of fluid
Symbol	Meaning
ρ	fluid density
u	fluid velocity, vector
p	pressure
μ	combined effective dynamic viscosity
μ_M	dynamic viscosity
μ_T	eddy viscosity
F_{st}	surface tension force, vector
g	acceleration from gravity, vector
k	turbulent kinetic energy
ϵ	turbulent dissipation
ϕ	phase-field variable
γ	phase-field interface mobility
G	Cahn–Hilliard free energy density
σ_{st}	surface tension coefficient
δ	phase-field interface thickness
$V_f^{\text{air}}, V_f^{\text{fluid}}$	volume fraction of air and fluid
J	molar flux density of NaCl brine, vector
c	molar concentration of NaCl brine
D_S	salt diffusion coefficient
c_{bulk}	bulk NaCl concentration of the concentrated jet
Q_0	volume flow rate of jet
R_{ch}, H_{ch}, L_j, d_0	dimensions of model geometry
Superscripts and subscripts.	
fluid	properties and variables characteristic of the fluid phase
air	properties and variables characteristic of the air phase
b	properties of NaCl brine
w	properties of water

1. Introduction

The plunging of a jet into another liquid body is a common phenomenon in both natural and industrial processes. The gaseous phase dragged by the impacting jet causes air to be entrained and dispersed into the receiving body. Along with aeration, this process leads to rapid mixing, promoted by the increased interfacial area between air and fluid phases. One common example of a plunging jet in nature is a waterfall. In natural waterfalls, aeration from the plunging jet enhances self-purification from organic pollutants [1,2]. Similarly, many environmental and industrial processes use plunging jets to enhance two-phase contact and mass transfer rates. Stirring of chemicals with plunging jets, for example, ensures good mixing between two liquids [3]. Plunging jets are also an inexpensive technology for oxygenation as a part of aerobic wastewater treatment processes [4]. Plunging jets can be used in fermentation [5], froth floatation [6], air pollution abatement [7], polymer [8], glass casting [9], and, recently, in brine dissolution processes [1,4].

Brine disposal has emerged as a major environmental challenge [10–12] as desalination technologies become central to sustaining public and industrial water sources [13]. The Arabian Gulf receives hypersaline brine discharged from Gulf Cooperation Council (GCC) countries at a rate as high as 40 million m³/day [14,15]. Along with reducing the amount of disposed brine products [16–21], addressing this problem requires us to investigate how these products travel throughout the local environment. Previous modeling and experimental work have demonstrated that far-field hydrodynamic processes such as tides, wind, and atmospheric exchange drive dispersion of discharge products across the marine ecosystem [22–25]. Meanwhile, small-scale transport plays a key role when we consider disposal strategies. Current disposal methods include sewer discharge [26], evaporation ponds [27], deep-well injection [28], land application [29], and surface water discharge [30,31].

In our previous work, we investigated plunging liquid jet reactors (PLJRs) as ejectors for disposed brine products from desalination plants [15,32,33]. In contrast with submerged jets in deep receiving water that have been the subject of most previous studies [34–39], PLJRs offer the ability to aerate and rapidly mix their dense ejecta into the receiving pool. Our results demonstrate that the use of PLJRs enhances the dilution of rejected brine and enriches the concentration of dissolved oxygen in the receiving water. Furthermore, compared to conventional aeration technologies, PLJRs perform these functions at a low cost [15,32,33].

In an unconfined PLJR (Fig. 1A), the liquid emerges from its nozzle as a high-speed jet that plunges from a height into a receiving pool of liquid. During this process, the jet entrains ambient air into the liquid pool in the shape of a conical downflow of bubbles. The sudden expansion of the jet upon impacting the receiving pool of liquid results in a short contact time between the bubbles and liquid [40,41]. This, in turn, limits the penetration depth of air bubbles. Additional structures may be incorporated into the PLJR to enhance the features of this process. For example, a downcomer tube may be added to the system to create a confined jet. This downcomer increases the superficial velocity of the jet and, with it, the momentum of two-phase flow. The downcomer also helps the jet and air bubbles penetrate to greater depths, improving air mass transfer and liquid mixing [41]. The annular-column PLJR, characterized by the addition of an annular column around the downcomer column, represents another mode of operation. The role of this structure is to segregate the ascending two-phase flow from the surrounding liquid. Ultimately, this configuration promotes higher mass transfer with no extra cost [40].

Currently, investigation of PLJRs is supported by empirical models [7]. However, the emergence of sophisticated computational tools has recently led to new advances in the field's theoretical understanding of plunging jets. These methods have allowed previous investigators to examine multiphase flow in the context of Navier–Stokes fluid transport. Approaches for describing the transport of discrete phases include Euler–Euler [42], mixture-model [43,44], phase-field [45,46], level-set [4,47–49], and Euler–Lagrange [47,50] formulations. The PLJR system is a turbulent, multi-phase, multi-physics problem, and it remains challenging to develop a predictive match between numerical simulations and experimental results. In particular, simulations tend to overestimate the volumetric rate of air entrainment in the falling jet [4]. Despite this limitation, previous efforts have successfully recapitulated important morphological features of the submerged gaseous phase [4]. In this paper, we study the unconfined PLJR process numerically and experimentally as a brine dispenser in order to examine the underlying processes.

One of the current limitations of PLJRs in a natural environment, is that the high-density of brine causes the jet to drop straight to the seafloor. As a result, there is very little convection-driven mixing, and dilution proceeds on the slow timescale of diffusion. The hypersaline, hypoxic phase remains concentrated on the seafloor [51–53] where it threatens the local marine ecosystem [54–56]. In our previous experimental work, we determined that the presence of brine in a plunging jet has an important influence on the system's fluid dynamics [15,32]. However, this element has not been incorporated as part of previous modeling efforts.

To suggest new insights for further improvement of the unconfined PLJR system, we have developed a volume of fluid (VOF) model that considers the co-transport of hypersaline brine. While multiphase mass transfer has been studied in a wide range of liquid–liquid and liquid–gas systems, the role of this process has not been studied as a part of the numerical simulation of plunging jets [57–61]. Similar to heat transfer [62], the motion of fluid influences the transport of dissolved brine, and, conversely, the presence of brine affects the flow of fluid. Our results suggest that these mechanisms are responsible for the concentration of hypersaline brine on the seafloor. As a part of this investigation, we also performed experiments for comparison under matching conditions. Our observations allowed us to outline several potential strategies for

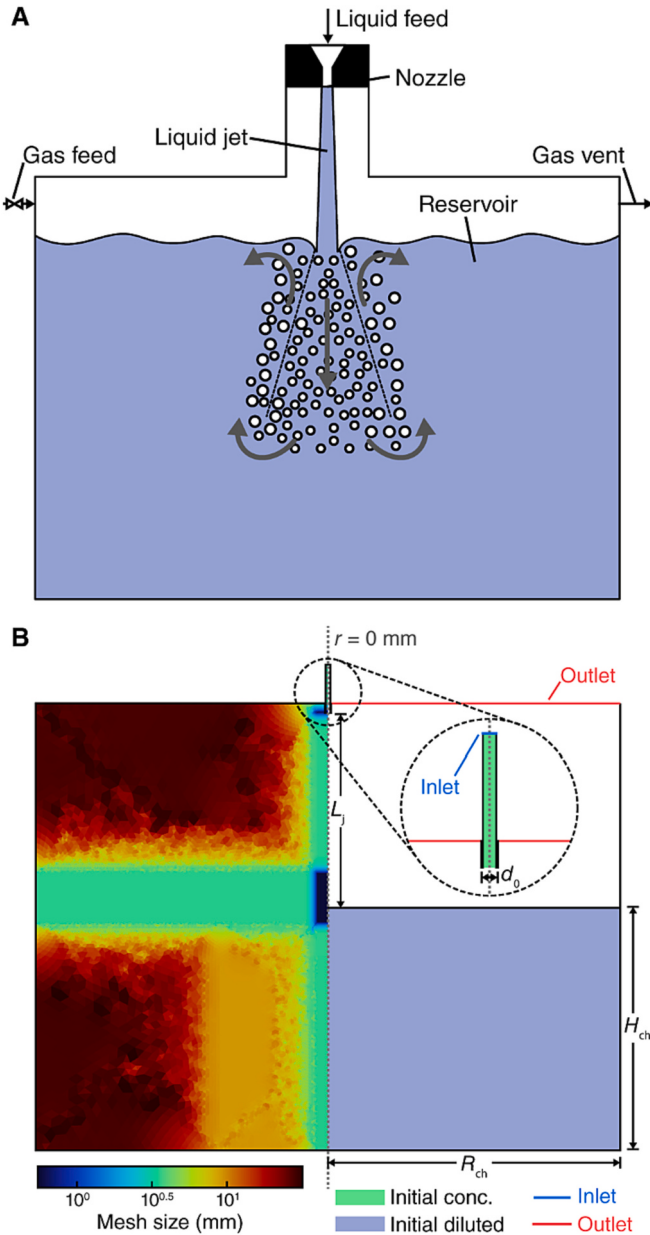


Fig. 1. An unconfined plunging jet system. (A) Schematic illustration of a plunging jet and components of our experimental setup. (B) Mesh element distribution (left) and model geometry (right). The geometry is two-dimensional and axisymmetric, with the axis of revolution labelled as $r = 0 \text{ mm}$. The boundary conditions (inlet, outlet, and walls), initial conditions (S_{init}), and model dimensions (R_{ch} , H_{ch} , L_j , and d_0) are discussed in Sec. 2.3.

disrupting the processes that lead to the negative effects of hypersaline brine impinging on the seafloor.

2. Materials and methods

We started by identifying a computationally tractable model that recapitulates the gravity-driven motion of brine. We used a phase-field model [45,46] to simulate the air–fluid multiphase transport and convection–diffusion equations to simulate the transport of brine. The constitutive equations and boundary conditions described in this section apply to the two-dimensional, axisymmetric geometry illustrated in Fig. 1B for cylindrical coordinates (r, z) .

2.1. Two-phase flow

The two-phase fluid–air interface was modeled according to the VOF approach [47,48,63]. This formulation used a single set of Navier–Stokes momentum equations to describe the viscous flow of fluids, with one velocity field calculated over the simulated volume. The volume fraction of each phase was solved from a separate continuity equation, which determined the material properties that Navier–Stokes depends on. Navier–Stokes can be written as

$$\rho \left(\frac{\partial \mathbf{u}}{\partial t} + \mathbf{u} \cdot \nabla \mathbf{u} \right) = -\nabla p + \nabla \cdot \mu (\nabla \mathbf{u} + \nabla \mathbf{u}^T) + \mathbf{F}_{\text{st}} + \rho \mathbf{g}, \quad (1)$$

where \mathbf{u} is the velocity field, ρ is the density, μ is the dynamic viscosity, p is the scalar pressure, \mathbf{g} is the acceleration due to gravity, and \mathbf{F}_{st} is the surface tension. For an incompressible fluid, the velocity field is divergence-free and follows

$$\nabla \cdot \mathbf{u} = 0 \quad (2)$$

The dynamic viscosity of the system was influenced both by the viscosity of the underlying phase mixture, μ_M , and the addition of turbulent viscosity, μ_T , according to

$$\mu = \mu_M + \mu_T \quad (3)$$

where μ_M is the viscosity of the underlying phase mixture and μ_T is the turbulent viscosity. Both μ_M and μ_T terms are calculated below. Similar to Refs. [4, 48, 49], the standard $k-\epsilon$ two-equation turbulence model was used to simulate sub-grid turbulence [64]. The first transport variable is the turbulent kinetic energy, k . Kinetic energy can be determined from the following equation:

$$\rho \left(\frac{\partial k}{\partial t} + \mathbf{u} \cdot \nabla k \right) = \nabla \cdot \left(\left(\mu_M + \frac{\mu_T}{\sigma_k} \right) \nabla k \right) + \mu_T (\nabla \mathbf{u} : (\nabla \mathbf{u} + \nabla \mathbf{u}^T)) - \rho \epsilon, \quad (4)$$

where $\sigma_k = 1$. The second transport variable is the rate of dissipation of turbulent kinetic energy, ϵ . Dissipation can be solved with the following equation:

$$\rho \left(\frac{\partial \epsilon}{\partial t} + \mathbf{u} \cdot \nabla \epsilon \right) = \nabla \cdot \left(\left(\mu_M + \frac{\mu_T}{\sigma_\epsilon} \right) \nabla \epsilon \right) + C_{1\epsilon} \frac{\epsilon}{k} \mu_T (\nabla \mathbf{u} : (\nabla \mathbf{u} + \nabla \mathbf{u}^T)) - C_{2\epsilon} \rho \frac{\epsilon^2}{k}, \quad (5)$$

where $\sigma_\epsilon = 1.3$, $C_{1\epsilon} = 1.44$, and $C_{2\epsilon} = 1.92$. Note that σ_k , σ_ϵ , $C_{1\epsilon}$, and $C_{2\epsilon}$ have arbitrary units, carrying their typical meaning in the standard $k-\epsilon$ model. Finally, according to the standard $k-\epsilon$ model, turbulent viscosity related to k and ϵ through

$$\mu_T = \rho C_\mu \frac{k^2}{\epsilon} \quad (6)$$

where $C_\mu = 0.09$.

For phase continuity, we applied the Cahn–Hilliard approach [45,46]. Here, interfacial diffusion fluxes were approximated as being proportional to chemical potential gradients. The convective Cahn–Hilliard equation is defined as

$$\frac{\partial \phi}{\partial t} + \mathbf{u} \cdot \nabla \phi = \gamma \nabla^2 G, \quad (7)$$

$$G = \frac{3\sigma_{\text{st}}}{\sqrt{8}} \left(-\delta \nabla^2 \phi + \frac{(\phi^2 - 1)\phi}{\delta} \right), \quad (8)$$

where ϕ is the dimensionless phase field variable that ranges from -1 in the fluid phase and 1 in the air phase, γ is the interface mobility, G is the free energy density, δ is the interfacial thickness, and σ_{st} is the surface tension coefficient. The phase field surface tension was then computed as a distributed force over the interface:

$$\mathbf{F}_{\text{st}} = G\nabla\phi. \quad (9)$$

We calculated the volume fractions, V_f^{air} and V_f^{fluid} , using the phase field variable:

$$V_f^{\text{air}} = \frac{(1 + \phi)}{2}, \quad (10)$$

$$V_f^{\text{fluid}} = \frac{(1 - \phi)}{2}. \quad (11)$$

We defined the material properties of the fluid in terms of these volume fractions:

$$\rho = \rho^{\text{air}} V_f^{\text{air}} + \rho^{\text{fluid}} V_f^{\text{fluid}}, \quad (12)$$

$$\mu_M = \mu^{\text{air}} V_f^{\text{air}} + \mu^{\text{fluid}} V_f^{\text{fluid}}. \quad (13)$$

For a plunging jet of brine, ρ^{fluid} was a function of the local solute concentration.

2.2. Brine co-transport

Here, we considered a binary electrolyte diffusing and convecting in aqueous media. Using the assumption of electroneutrality, we restricted our dependent variables to a single concentration, c [65]. The time-varying behavior of the solute was dictated by continuity, which is given in this case as:

$$\frac{\partial c}{\partial t} = -\nabla \cdot \mathbf{J}, \quad (14)$$

where \mathbf{J} , and c are the molar flux density and molar concentration respectively of NaCl. Chemical flux from diffusion and convection is given by the following equation for dilute solutions:

$$\mathbf{J} = V_f^{\text{fluid}} (-D_S \nabla c + c\mathbf{u}), \quad (15)$$

where D_S is the salt diffusivity of NaCl.

The density of the fluid, ρ^{fluid} , was dependent on the concentration of brine (NaCl) according to

$$\rho^{\text{fluid}} = \rho^b \frac{c}{c_{\text{bulk}}} + \rho^w, \quad (16)$$

where c_{bulk} is the bulk NaCl concentration of the concentrated jet, ρ^w is the density of pure water, and ρ^b is the density of NaCl when $c = c_{\text{bulk}}$.

2.3. Boundary and initial conditions

The boundaries of the model geometry are illustrated in Fig. 1B. At the inlet, the fluid was given constant velocity:

$$u_z|_{\text{inlet}} = -\left(\frac{4Q_0}{\pi d_0^2}\right), \quad (17)$$

where u_z is the vertical component of fluid velocity (\mathbf{u}), Q_0 is the volume flow rate at the inlet, and d_0 is the inlet diameter. This boundary was also fixed to the fluid phase with brine concentration:

$$c|_{\text{inlet}} = c_{\text{bulk}}, \quad (18)$$

$$\phi|_{\text{inlet}} = -1, \quad (19)$$

where c_{bulk} is the NaCl concentration of the incoming jet. At the outlet, the fluid was set at a fixed pressure relative to hydrostatic pressure:

$$p|_{\text{outlet}} = \rho g_z z, \quad (20)$$

where g_z is acceleration due to gravity and z is the vertical position in the tank (the tank floor is set to $z = 0$ mm). The phase and concentration at

this boundary were set as outflows. Finally all other walls were impermeable, had no slip, and met the fluid at a contact angle of 90°.

The initial conditions for each simulation are illustrated in Fig. 1B. The inlet region was filled with fluid ($V_f^{\text{fluid}} = 1$) at brine concentration ($c = c_{\text{bulk}}$). The reservoir region was filled with fluid ($V_f^{\text{fluid}} = 1$) without salinity ($c = 0 \text{ mol/m}^3$). All other regions were filled with air ($V_f^{\text{fluid}} = 0$, $c = 0 \text{ mol/m}^3$).

1.1. Parameters

The parameters used in these simulations were based on the ones applied in our experimental work [15,32]. Unless specified otherwise, the parameters can be found in Table 1.

2.4. Numerical details

A regular grid of 670 μm rectangular elements was used to mesh the model in the regions where air–fluid transitions occurred. Specifically, this mesh density was used in the vicinity of the jet, plume, and reservoir surface. In the remaining areas, a triangular mesh with a maximum element size of 21 mm was applied. In COMSOL Multiphysics, we used the segregated solver to couple the dependent variables. To reach convergence, the dependent variables were added in three steps: (1) velocity, pressure, and the phase-field variable; (2) turbulence variables; and (3) brine concentration.

2.5. Experimental details

To verify the behaviors observed in our simulation, we designed and constructed a model unconfined PLJR system (see Fig. 2). The system, adapted from our previous work, was designed as a scale model of an outfall system [15,32,33]. The dimensions of this system were as follows: $L = 2 \text{ m}$, $W = 1 \text{ m}$, $H = 1.2 \text{ m}$. The nozzle was designed with a diameter of $d_0 = 10 \text{ mm}$ (nozzle length to diameter ratio of 5, similar to Refs. [66, 67]). The nozzle was placed $L_j = 20 \text{ cm}$ and 40 cm from the receiving water body, whose level we set at $H_{\text{ch}} = 50 \text{ cm}$.

Water was continuously withdrawn from the base of a reservoir by a centrifugal pump, recycled through rotameters, and driven through the nozzle as a jet plunging into the same reservoir. The role of the rotameters in this setup was to measure flowrate. In our experiments, we drove fluid at volumetric flow rates of $Q_0 = 300 \text{ L/hr}$ and $Q_0 = 576 \text{ L/hr}$.

The experimental jet system can be scaled to prototype levels using Froude scaling. If we take a desalination plant with a single outfall producing $Q_{\text{plant}} = 300 \text{ m}^3/\text{hr}$, we will have a volume ratio of $Q_{\text{plant}}/Q_0 = 1000$ when we compare it to our scale model with $Q_0 = 300 \text{ L/hr}$. As calculated in Ref. [15], the size of the system would scale to a field prototype according to $L_r = (Q_{\text{plant}}/Q_0)^{0.4} = 15.84$. Thus, the receiving water depth of 50 cm and nozzle diameter of 1 cm would scale from laboratory dimensions as 7.92 m and 15.8 cm respectively.

The fluid emerging from the jet contained an NaCl solution with $c_{\text{bulk}} = 683.06 \text{ mol/m}^3$, and the receiving pool initially contained no

Table 1
Simulation parameters.

$D_S (\text{m}^2/\text{s})$	$c_{\text{bulk}} (\text{mol/m}^3)$	$L_j (\text{cm})$	$d_0 (\text{cm})$	$R_{\text{ch}} (\text{cm})$	$H_{\text{ch}} (\text{cm})$	$Q_0 (\text{L/h})$
1.35×10^{-9}	683.06	40	1	60	50	300
$\rho^b (\text{kg/m}^3)$	$\rho^{\text{air}} (\text{kg/m}^3)$	$\rho^w (\text{kg/m}^3)$	$\mu^{\text{air}} (\text{Pa}\cdot\text{s})$	$\mu^{\text{fluid}} (\text{Pa}\cdot\text{s})$	$\sigma_{\text{st}} (\text{N/m})$	$\delta (\text{mm})$
1029	1.185	998	1.831×10^{-5}	1.068×10^{-3}	0.074	1
						1×10^{-6}

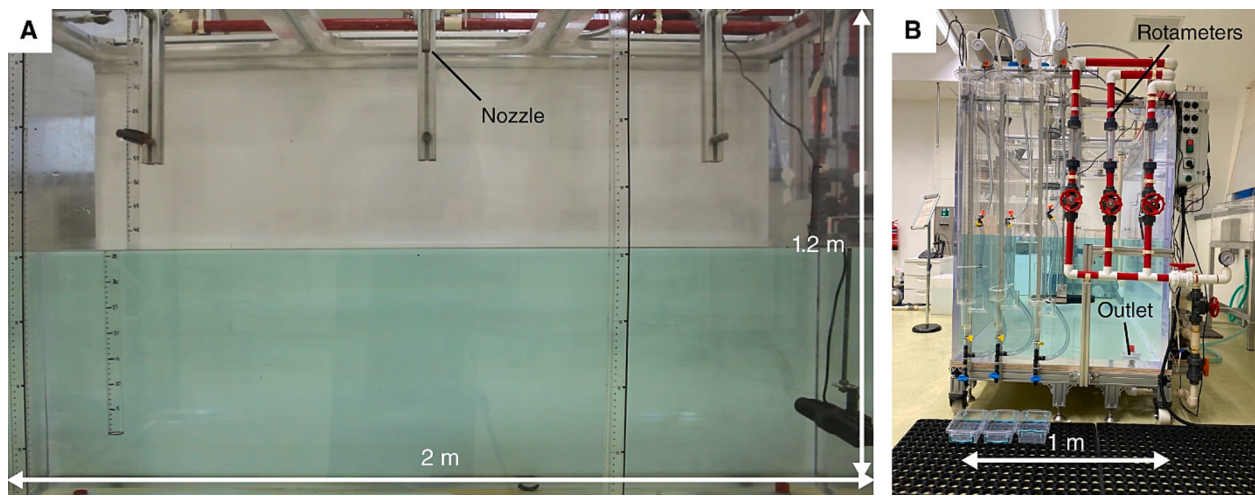


Fig. 2. Experimental unconfined plunging liquid jet reactor system. (A) Front view. (B) Side view.

solutes ($c_{\text{bulk}} = 0 \text{ mol/m}^3$). A red dye was added to the plunging salt solution as a visual proxy for salt concentration, allowing us to view the trajectory of the two-phase mixture below the receiving pool after the jet's impact. We carried out each experiment for a duration of at least 50 s.

3. Results and discussion

3.1. Air entrainment and cavity formation

A falling jet entrains air within the rough features of its interface and drags a boundary layer of air in its wake [7,9]. This air then impacts the fluid reservoir in an annular region surrounding the falling jet, causing the transport of air into the reservoir [68]. As with previous numerical studies [4,42–49], our simulation recapitulated the key characteristics of this process. As shown in Fig. 3A, the surface tension of the fluid caused air cavities to form in the plume surrounding the impacted volume. Due to the large gradient in velocity at the impact site, quantified by the rate-of-strain tensor, significant sub-scale turbulence was generated at this location. This, in turn, caused the effective viscosity of the fluid to increase at the base of the developing plume. Ultimately, this phenomenon limited the plunging depth. Despite the momentum carried by the jet plunging from 40 cm, we see in Fig. 3A that the air cavity only reached ~20 cm below the surface of the reservoir. When we removed

the effect of turbulence from our model, we observed that the plume reached the floor of the reservoir.

Along with this main cavity of air, the impacting jet generated sub-grid air bubbles that were represented in our model as diffuse volumes of a fluid-air mixture. To understand the trajectories of individual bubbles within this volume, we employed the Euler-Lagrange particle tracking approach (see Sec. SM-1 of the Supplementary Material). Fig. 3B illustrates the trajectories of three bubble diameters: 0.1 mm, 1 mm, and 4 mm. As expected, smaller bubbles traveled deeper into the reservoir and spread out radially from the plume. From the central cavity, air absorbed into the fluid and diffused in small concentrations throughout the plume.

While the geometry of the plume matched up with experimental results [15], there was less consistency with the volumetric rate of air entrainment. Our simulation overpredicted the air entrainment rate by an order of magnitude (see Sec. SM-2 of the Supplementary Material). As discussed in Bahadar et al., this problem is endemic to the numerical simulation of plunging jets [4].

3.2. Brine transport

The transport of the dissociated brine was governed by diffusion and convection in our system. As shown in Fig. 4, convection occurred on a much faster timescale than diffusion, causing the brine to primarily follow the velocity field of the underlying fluid. When solute diffusion

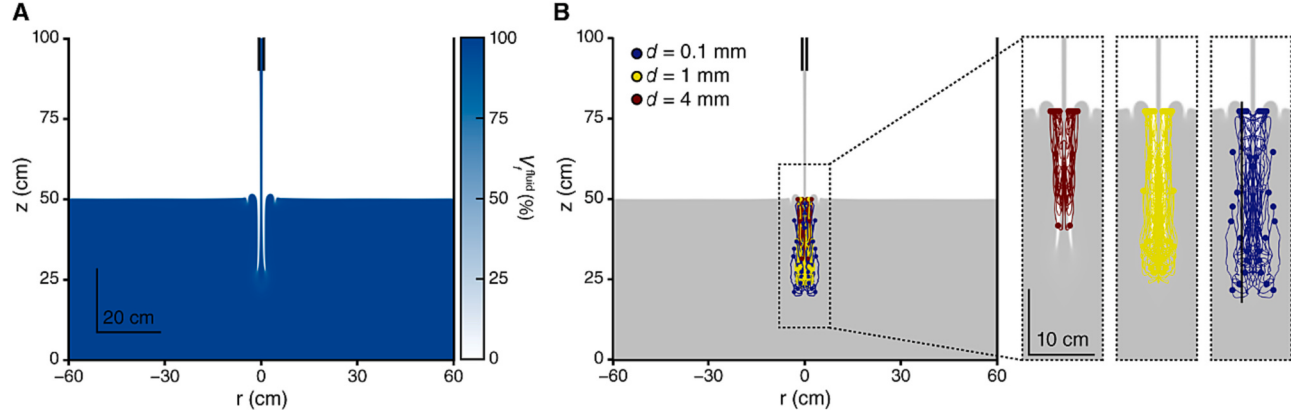


Fig. 3. Air transport within an unconfined plunging jet system. For this simulation, $L_j = 40 \text{ cm}$ and $Q_0 = 576 \text{ L/hr}$. For other model parameters, see Fig. 1B and Table 1. (A) Volume fraction of fluid relative to air at steady-state. (B) Euler-Lagrange particle tracking of bubbles having three different diameters over an interval of $\Delta t = 4 \text{ s}$. Over this period, 40 bubbles were released at $z = 0.5 \text{ m}$ on a disk of radius of 22 mm. The probability of being released at a particular location was weighted by its proximity to the air-fluid interface.

was removed from the system by setting $D_s \rightarrow 0 \text{ m}^2/\text{s}$, we observed that the brine follows an identical profile for all conditions we examined.

Because diffusion occurs on a slow timescale, the brine remained concentrated as it plunged into the reservoir. In Fig. 4A, we see that the brine followed the underlying envelope of the plume—it traveled vertically downwards, wrapped radially around the base of the plume, and then rose back to the surface. Meanwhile, in Fig. 4B, the brine only followed the original plume for the first 5 s of the simulation. After that, it dropped straight downwards until it reached the floor of the tank. In summary, we observed two distinct regimes: (Regime 1) the brine followed the original plume in the radial direction (Fig. 4A), and (Regime 2) the brine dropped straight downwards from the plume (Fig. 4B). Under the conditions studied here, their respective regimes persisted until the end of the simulations ($t = 100 \text{ s}$). For designing a desalination outfall system, the radial mixing characterizing Regime 1 (Fig. 4A) represents an ideal target from an environmental perspective. In Regime 2 (Fig. 4B), on the other hand, we see that the brine persisted as hypersaline media as is spread along the floor. As previously discussed,

when this process develops along the seafloor, it leads to deterioration of the local ecosystem.

3.3. Interplay between air and brine

In this model, the composition of air and brine in the fluid both contributed to its density. As shown in the buoyancy plots of Fig. 4, volumes of low density were created around the plumes where air became entrained. At $t = 1 \text{ s}$ for both Fig. 4A and B, we see that all of the fluid followed the profile of the plume and rose towards the surface of the reservoir immediately after plunging. The jet salinities of both Fig. 4A and B were the same, and they both entrained a similar volume of air (see Fig. SM-1). Despite this, the jets impacted their reservoirs with opposite buoyancies. This occurred because the slower jet speed in Fig. 4A gave the air time to diffuse throughout the jet before it impacted. Meanwhile, the center of the jet in Fig. 4B remained dense as it plunged, and it traveled deeper into the reservoir since the center carried more velocity. As a result, at $t = 5 \text{ s}$ in Fig. 4B, we see that the denser fluid

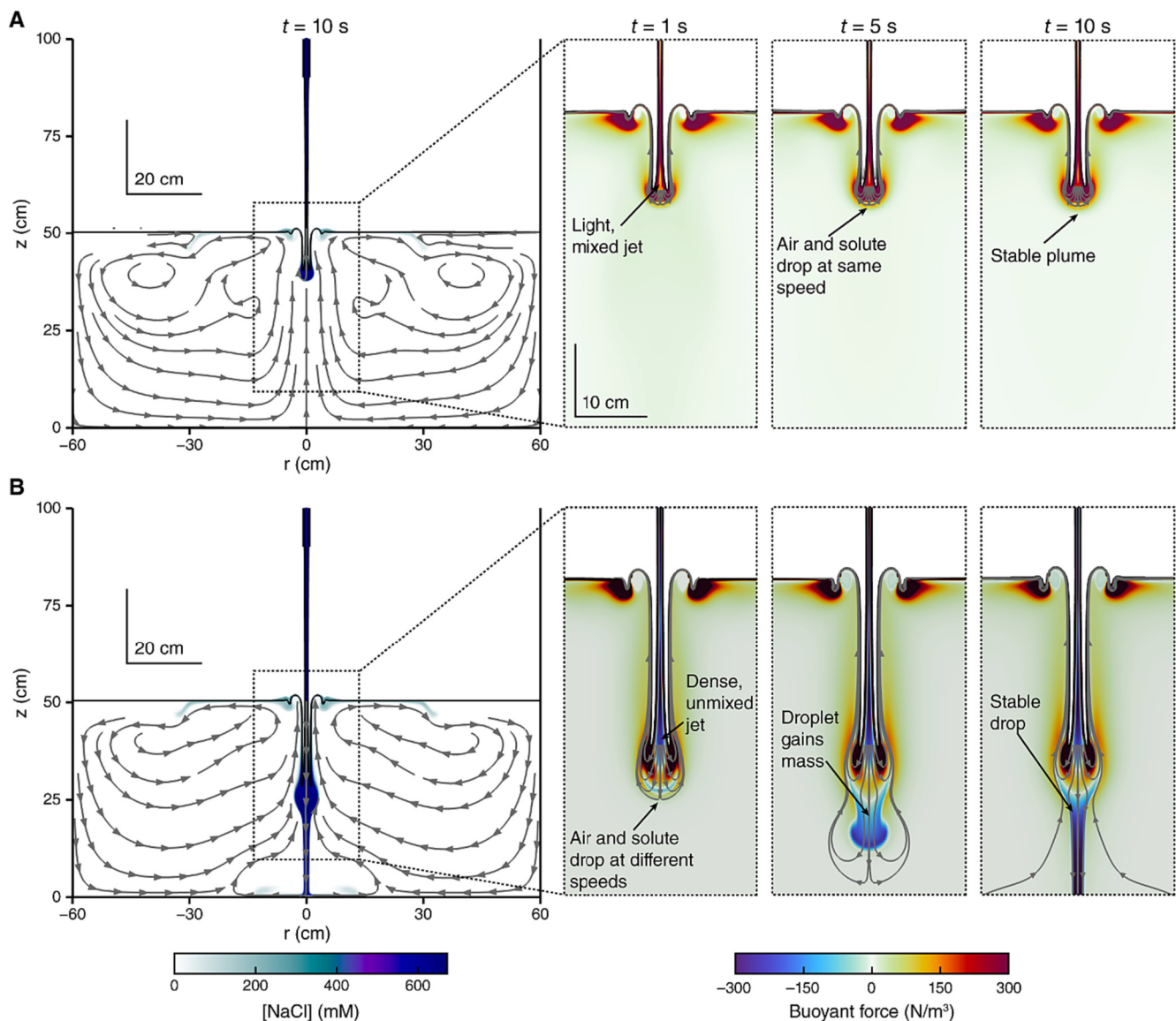


Fig. 4. Simulated transport within an unconfined PLJR system. The colormap on the left corresponds to the concentration of NaCl brine ($[NaCl] = c$), and the colormap on the right corresponds to the force of buoyancy. The gray lines are streamlines of fluid velocity, and their arrows indicate the direction of the field across those lines. The black line shows the contour of the volume fraction of the fluid. For other model parameters, see Fig. 1B and Table 1. (A) $L_j = 40 \text{ cm}$, $Q_0 = 300 \text{ L/hr}$. (B) $L_j = 40 \text{ cm}$, $Q_0 = 576 \text{ L/hr}$.

accumulated at the base of the plume as a heavy droplet. The droplet began to detach from the plume, and finally, by $t = 10$ s, it fell to the floor of the reservoir. As it fell, it dragged the rest of the plunging fluid down with it, causing a steady flow of brine to impinge upon the floor. At the same time, part of the jet's plume continued to flow upwards, driven by the air captured in the plunge. For the jet in Fig. 4A, we see that the heavy droplet never formed or detached. These behaviors persisted indefinitely beyond $t = 100$ s into our simulation.

As shown in Figs. 5 and 6, the key predictions of these simulations were recapitulated by our scale experiments. For $Q_0 = 300$ L/hr (Figs. 5A and 6A), the brine followed the original plume back towards the surface of the reservoir. In this case, we see that the brine primarily mixed radially outwards from the plume. Meanwhile, for $Q_0 = 576$ L/hr (Figs. 5B and 6B), we see that the brine dropped straight downwards and mixed primarily along the longitudinal axis. In contrast with our

simulations, the brine appears to diffuse more rapidly away from the concentrated stream. This most likely occurred as a result of bulk convection processes such as thermal currents that arise in natural systems [69]. To see our full experiments (each carried out for at least 50 s durations), please see the videos in our Supplementary Material. Overall, both simulated and experimental results suggest that the flow rate of the jet was one of the key parameters that influenced the behavior of the system and that we can promote radial mixing by reducing it.

Both the simulation and experiment suggest that a finite volume of fluid rose from the bottom of the air cavity to the pool surface where it spread radially. The significant of this phenomenon, is that the rising fluid mixed with the surrounding fluid much more effectively. Therefore, it offers a potential mechanism for improving the dilution of plunging jet outfalls: to prevent most of the fluid from sinking to the floor of the reservoir, we can enhance the positive buoyancy of fluid

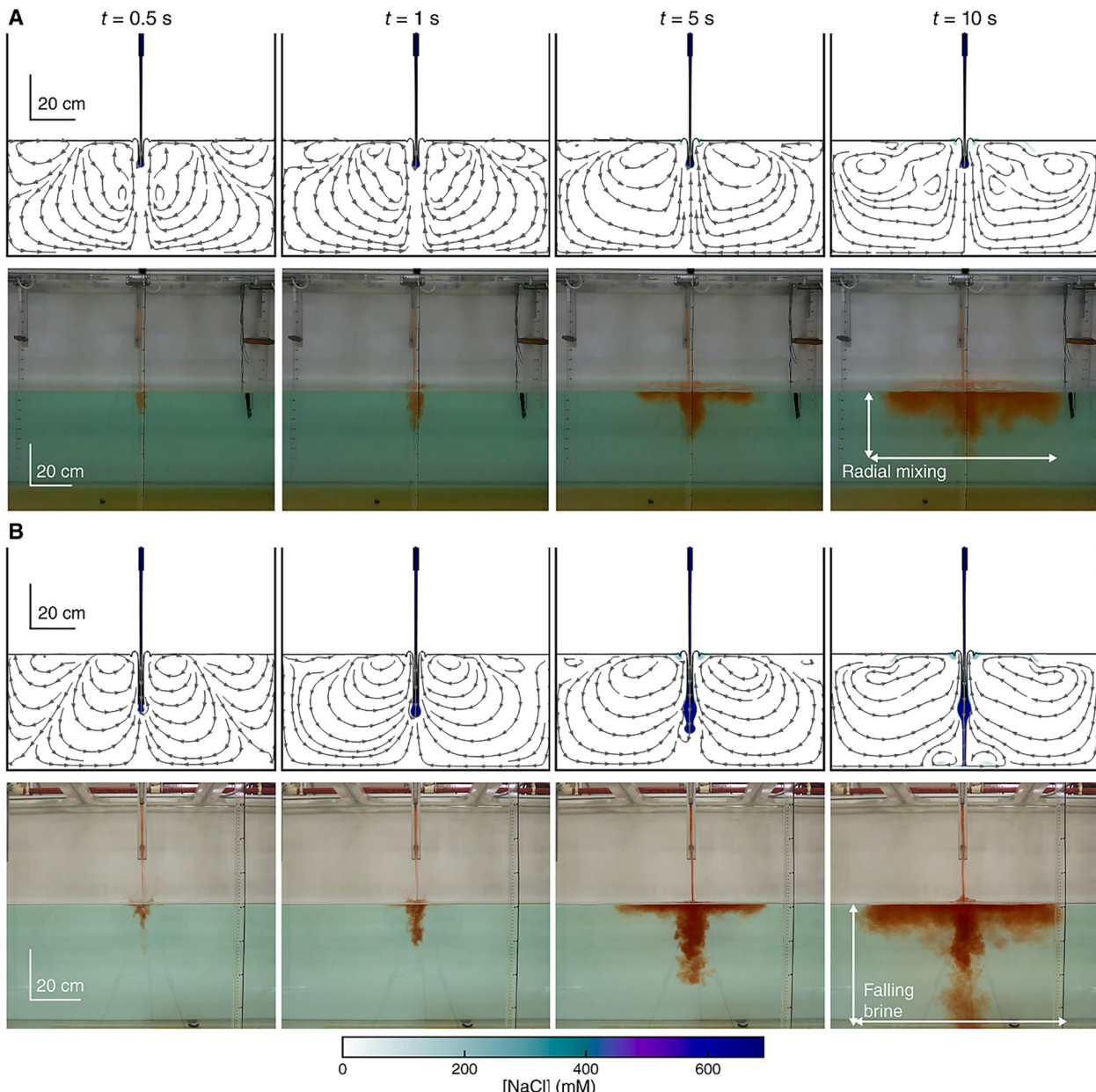


Fig. 5. Solute transport within an unconfined PLJR system for $L_j = 40$ cm. The top rows display simulation results, while the bottom rows display frames taken from plunging jet experiments. This study used a fluorescent red dye as a tracer for the high-salinity brine driven by the jet. The colormap corresponds to the simulated concentration of NaCl brine ($[NaCl] = c$). The gray arrows are streamlines of fluid velocity, and the black line shows the contour of the volume fraction of the fluid. For other model parameters, see Fig. 1B and Table 1. (A) $Q_0 = 300$ L/hr. (B) $Q_0 = 576$ L/hr.

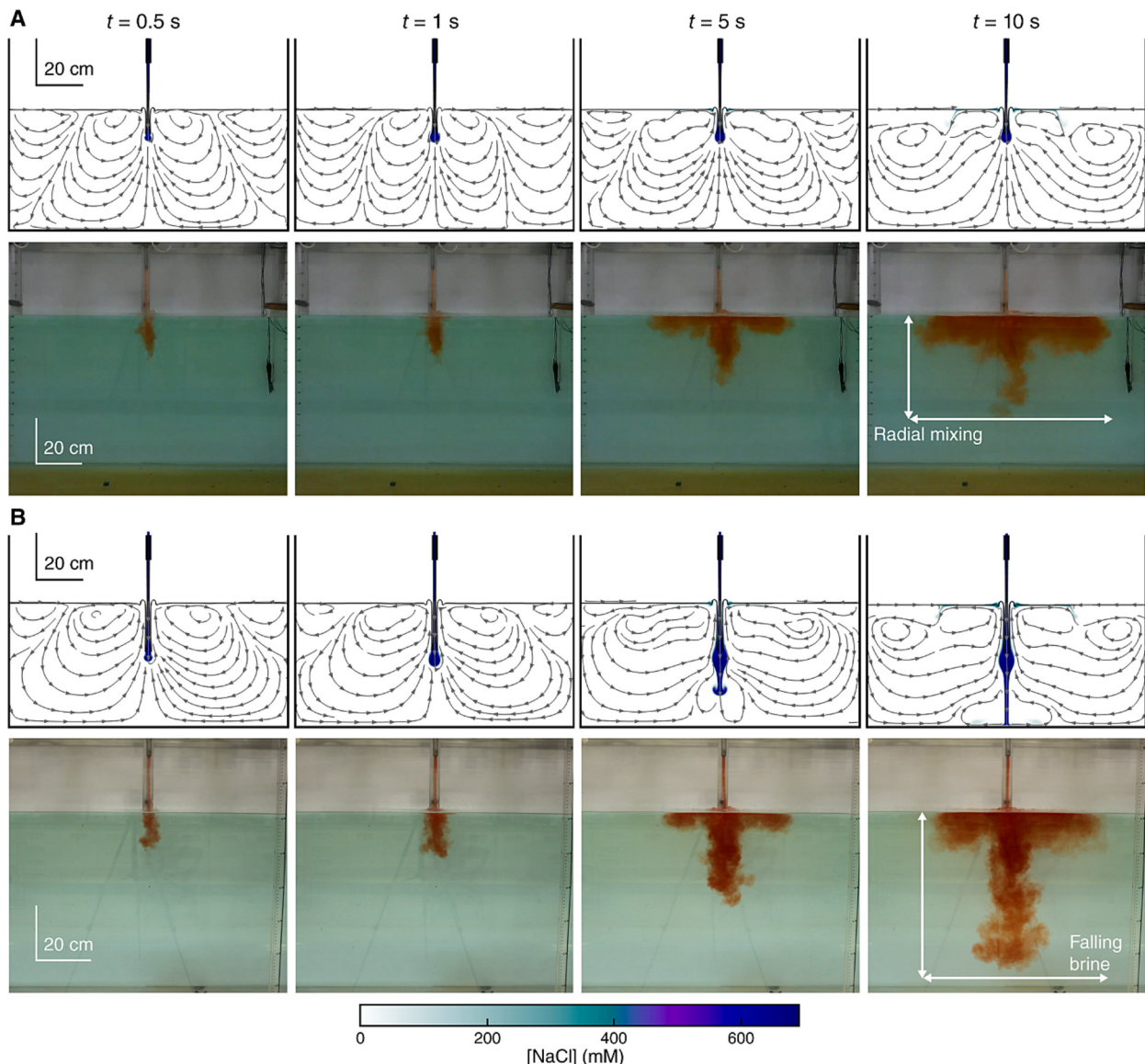


Fig. 6. Solute transport within an unconfined PLJR system for $L_j = 20$ cm. The top rows display simulation results, while the bottom rows display frames taken from plunging jet experiments. This study used a fluorescent red dye as a tracer for the high-salinity brine driven by the jet. The colormap corresponds to the simulated concentration of NaCl brine ($[NaCl] = c$). The gray arrows are streamlines of fluid velocity, and the black line shows the contour of the volume fraction of the fluid. For other model parameters, see Fig. 1B and Table 1. (A) $Q_0 = 300$ L/hr. (B) $Q_0 = 576$ L/hr.

emerging from the plume. However, our results show that increasing the ratio between air entrainment rate and brine ejection rate will not necessarily prevent the formation of a heavy droplet. Along with introducing more air into the plume, the jet needs to be optimized so that the air permeates it before impact. Based on our simulations and experiments, this can be achieved by increasing jet length (L_j), decreasing jet flow rate (Q_0), and decreasing nozzle diameter (d_0).

Our results suggest that the entrainment of air in the impacting jet can prevent the gravity-driven drop of high-density brine when the air is distributed throughout the jet's cross-sectional area. The falling and rising state are both stable attractors of the system under the different flow regimes. The falling state was the only stable state observed under fast flow rate conditions, and the radial mixing state was the only state observed under slow flow rate conditions. When the model was simulated under slow conditions and then switched to fast conditions, it reverted back to the radial mixing regime. Therefore, the falling state is not irreversible in our simulations.

4. Conclusions

In this study, we applied the finite element method to study multiphase flow in a plunging jet system. We used a phase-field approach to better understand the momentum transfer between the two phases, and we used a particle-tracking method to visualize the trajectories of individual bubbles entrained by the falling jet. We found that the plume geometry of the entrained air matched closely with experimental results.

Ultimately, the purpose of this study was to understand the co-transport of brine in the plunging jet system. In our model, Navier–Stokes described the transport of fluid, and Nernst–Planck described transport of dissolved brine. These two processes were coupled to each other through convection and buoyancy. We determined that brine transport was convection-driven, with minor influence from diffusion on brine trajectory. We found that two distinct behaviors emerged depending on the jet's characteristics. We found that these behaviors persisted indefinitely in our simulations and experiments. Depending on

the jet flow rate, the brine would either (1) follow the original plume in the radial direction or (2) drop straight downwards from the plume. In our experiments, we observed the same behaviors. We also observed that those behaviors diverged under the same flow rate conditions simulated in our model.

To understand the processes that gave rise to those behaviors, we examined buoyant forces acting on the plume. Our model demonstrated that air and brine, driven by the underlying velocity field, were transported non-uniformly throughout the plume. Since the density of the fluid is dependent on local composition of air and brine, the plunging jet induced volumes of both negative and positive buoyancy. Ultimately, we determined that the distribution of buoyant forces gave rise to the distinct regimes observed in our simulation. Crucially, brine trajectory was not only influenced by the total rate of air entrainment but also by the distribution of air within the impacting jet.

Since we were able to reproduce distinct regimes in our scale experiments under conditions matching our simulations, we propose that the same mechanisms were involved. However, it would be valuable to further investigate the underlying role of buoyancy in future efforts. It would also be valuable to understand how the behaviors we observed might be influenced by a real marine environment and its characteristic processes. Relevant aspects may include interaction between multiple jets and the presence of lateral flow, as we investigated in our previous experimental work [15,32,33].

Based on insight from our model, we found that it may be possible to avoid destructive outcomes by maintaining the jet system in its radial mixing regime. Understanding the trajectory of brine in outfall systems will help us avoid the deterioration of marine ecosystems. More broadly, our results might lend insight into plunging jet systems that we encounter in our daily lives, such as waterfalls.

This article references a supplementary material section containing additional modeling details and figures. In addition, we provide videos of the experiments we carried out as part of this work. Supplementary data to this article can be found online at doi:<https://doi.org/10.1016/j.desal.2023.116996>.

Funding

This research was funded by Kuwait Foundation for Advancement of Sciences, grant number PN1815EV07.

CRediT authorship contribution statement

Matthew T. Flavin: Conceptualization, Methodology, Software, Validation, Formal analysis, Investigation, Writing – original draft. **Jenifer Fernandes:** Validation, Investigation, Writing – review & editing. **Rawan AlQabandi:** Validation, Investigation, Writing – review & editing. **Eric Adams:** Conceptualization, Writing – review & editing. **Jongyoon Han:** Conceptualization, Writing – review & editing, Supervision, Project administration, Funding acquisition. **Bader Al-Anzi:** Conceptualization, Writing – review & editing, Supervision, Project administration, Funding acquisition.

Declaration of competing interest

The authors declare that they have no known competing financial interests or personal relationships that could have appeared to influence the work reported in this paper.

Data availability

Data will be made available on request.

References

- [1] B.S. Al-Anzi, J. Fernandes, Sensitivity test of jet velocity and void fraction on the prediction of rise height and performance of a confined plunging liquid jet reactor, *Processes* 10 (2022), <https://doi.org/10.3390/pr10010160>.
- [2] M. Saito, Y. Magara, Wisjuprapto, study on self-purification capacity for organic pollutants in stagnant water, *Water Sci. Technol.* 46 (2002) 137–145, <https://doi.org/10.2166/wst.2002.0224>.
- [3] T. Bagatur, A. Baylar, N. Sekerdag, The effect of nozzle type on air entrainment by plunging water jets, *Water Qual. Res. J. Canada.* 37 (2002) 599–612, <https://doi.org/10.2166/wqrj.2002.040>.
- [4] A. Bahadar, Volume of fluid computations of gas entrainment and void fraction for plunging liquid jets to aerate wastewater, *ChemEngineering.* 4 (2020) 1–19, <https://doi.org/10.3390/chemengineering4040056>.
- [5] P.R. Fields, F.R.G. Mitchell, N.K.H. Slater, Studies of mixing in a concentric tube air-lift reactor containing xanthan gum by means of an improved flow follower, *Chem. Eng. Commun.* 25 (1984) 93–104, <https://doi.org/10.1080/00986448408940100>.
- [6] P. Ireland, R. Cunningham, G.J. Jameson, The behaviour of wash water injected into a froth, *Int. J. Miner. Process.* 84 (2007) 99–107, <https://doi.org/10.1016/j.minpro.2006.08.007>.
- [7] A.K. Biñ, Gas entrainment by plunging liquid jets, *Chem. Eng. Sci.* 48 (1993) 3585–3630, [https://doi.org/10.1016/0009-2509\(93\)81019-R](https://doi.org/10.1016/0009-2509(93)81019-R).
- [8] A.V. Subbotin, I.Y. Skvortsov, M.S. Kuzin, P.S. Gerasimenko, V.G. Kulichikhin, A. Y. Malkin, The shape of a falling jet formed by concentrated polymer solutions, *Phys. Fluids* 33 (2021), <https://doi.org/10.1063/5.0060960>.
- [9] M. Song, K.S. Ball, T.L. Bergman, A model for radiative cooling of a semitransparent molten glass jet, *J. Heat Transfer* 120 (1998) 931–938, <https://doi.org/10.1115/1.2825912>.
- [10] A. Panagopoulos, Water-energy nexus: desalination technologies and renewable energy sources, *Environ. Sci. Pollut. Res.* (2021), <https://doi.org/10.1007/s11356-021-13332-8>.
- [11] N. Kress, Marine Impacts of Seawater Desalination: Science, Management, and Policy, 2019, <https://doi.org/10.1016/C2016-0-01997-6>.
- [12] N. Kress, Y. Gertner, E. Shoham-Fridor, Seawater Quality at the Brine Discharge Site from Two Mega Size Seawater Reverse Osmosis Desalination Plants in Israel, Eastern Mediterranean, *Water Res.* 2020, <https://doi.org/10.1016/j.watres.2019.115402>.
- [13] A. Panagopoulos, K.J. Haralambous, Minimal Liquid Discharge (MLD) and Zero Liquid Discharge (ZLD) Strategies for Wastewater Management and Resource Recovery-Analysis, Challenges and Prospects, *J. Environ. Chem. Eng.* 2020, <https://doi.org/10.1016/j.jece.2020.104418>.
- [14] W.J.F. Le Quesne, L. Fernand, T.S. Ali, O. Andres, M. Antonpoulou, J.A. Burt, W. W. Dougherty, P.J. Edson, J. El Kharraz, J. Glavan, R.J. Mamit, K.D. Reid, A. Sajwani, D. Sheahan, Is the development of desalination compatible with sustainable development of the Arabian gulf? *Mar. Pollut. Bull.* (2021) <https://doi.org/10.1016/j.marpolbul.2021.112940>.
- [15] A.C. Chow, I. Shrivastava, E.E. Adams, F. Al-Rabaie, B. Al-Anzi, Unconfined dense plunging jets used for brine disposal from desalination plants, *Processes* 8 (2020), <https://doi.org/10.3390/PR8060696>.
- [16] Y. Oren, E. Korngold, N. Daltrophe, R. Messalem, Y. Volkman, L. Aronov, M. Weismann, N. Bouriakov, P. Glueckstern, J. Gilron, Pilot Studies on High Recovery BWRO-EDR for near Zero Liquid Discharge Approach, *Desalination*, 2010, <https://doi.org/10.1016/j.desal.2010.06.010>.
- [17] A. Panagopoulos, Techno-economic assessment of minimal liquid discharge (MLD) treatment systems for saline wastewater (brine) management and treatment, *Process. Saf. Environ. Prot.* (2021), <https://doi.org/10.1016/j.psep.2020.12.007>.
- [18] A. Panagopoulos, Beneficiation of Saline Effluents from Seawater Desalination Plants: Fostering the Zero Liquid Discharge (ZLD) Approach - A Techno-Economic Evaluation, *J. Environ. Chem. Eng.* 2021, <https://doi.org/10.1016/j.jece.2021.105338>.
- [19] H. Dahmardeh, H.A. Akhlaghi Amiri, S.M. Nowee, Evaluation of mechanical vapor recompression crystallization process for treatment of high salinity wastewater, *Chem. Eng. Process. - Process Intensif.* (2019), <https://doi.org/10.1016/j.cep.2019.107682>.
- [20] F.E. Titchou, H. Zazou, H. Afanga, J. El Gaayda, R. Ait Akbour, P.V. Nidheesh, M. Hamdani, Removal of organic pollutants from wastewater by advanced oxidation processes and its combination with membrane processes, *Chem. Eng. Process. - Process Intensif.* (2021), <https://doi.org/10.1016/j.cep.2021.108631>.
- [21] A. Panagopoulos, Brine management (saline water & wastewater effluents): Sustainable utilization and resource recovery strategy through Minimal and Zero Liquid Discharge (MLD & ZLD) desalination systems, *Chem. Eng. Process. - Process Intensif.* (2022), <https://doi.org/10.1016/j.cep.2022.108944>.
- [22] Z. Lachkar, M. Mehari, M. Lévy, F. Paparella, J.A. Burt, Recent expansion and intensification of hypoxia in the Arabian Gulf and its drivers, *Front. Mar. Sci.* (2022), <https://doi.org/10.3389/fmars.2022.891378>.
- [23] F. Yao, W.E. Johns, A HYCOM modeling study of the Persian Gulf: 1. Model configurations and surface circulation, *J. Geophys. Res. Ocean.* (2010), <https://doi.org/10.1029/2009JC005781>.
- [24] A.C. Chow, W. Verbruggen, R. Morelissen, Y. Al-Osairi, P. Ponnunani, H.M. S. Lababidi, B. Al-Anzi, E.E. Adams, Numerical Prediction of Background Buildup of Salinity Due to Desalination Brine Discharges into the Northern Arabian Gulf, *Water (Switzerland)*, 2019, <https://doi.org/10.3390/w11112284>.
- [25] D.A. Botelho, M.E. Barry, G.C. Collecutt, J. Brook, D. Wiltshire, Linking near- and far-field hydrodynamic models for simulation of desalination plant brine discharges, *Water Sci. Technol.* (2013), <https://doi.org/10.2166/wst.2013.673>.

- [26] R. Katal, T. Ying Shen, I. Jafari, S. Masudy-Panah, M. Hossein Davood Abadi Farahani, An overview on the treatment and management of the desalination brine solution, Desalin. - Challenges Oppor. (2020), <https://doi.org/10.5772/intechopen.92661>.
- [27] M. Ahmed, W.H. Shayya, D. Hoey, A. Mahendran, R. Morris, J. Al-Handaly, Use of Evaporation Ponds for Brine Disposal in Desalination Plants, Desalination, 2000, [https://doi.org/10.1016/S0011-9164\(00\)00083-7](https://doi.org/10.1016/S0011-9164(00)00083-7).
- [28] K.P. Saripalli, M.M. Sharma, S.L. Bryant, Modeling injection well performance during deep-well injection of liquid wastes, J. Hydrol. (2000), [https://doi.org/10.1016/S0022-1694\(99\)00164-X](https://doi.org/10.1016/S0022-1694(99)00164-X).
- [29] A. Panagopoulos, K.J. Haralambous, M. Loizidou, Desalination brine disposal methods and treatment technologies - a review, Sci. Total Environ. (2019), <https://doi.org/10.1016/j.scitotenv.2019.07.351>.
- [30] K.C. Kornelsen, P. Coulibaly, Synthesis review on groundwater discharge to surface water in the Great Lakes Basin, J. Great Lakes Res. (2014), <https://doi.org/10.1016/j.jglr.2014.03.006>.
- [31] I. Shrivastava, E.E. Adams, Pre-dilution of desalination reject brine: impact on outfall dilution in different water depths, J. Hydro-Environment Res. (2019), <https://doi.org/10.1016/j.jher.2018.09.001>.
- [32] I. Shrivastava, E.E. Adams, B. Al-Anzi, A.C. Chow, J. Han, Confined plunging liquid jets for dilution of brine from desalination plants, Processes 9 (2021), <https://doi.org/10.3390/pr9050856>.
- [33] B. Al-Anzi, Application of Confined Plunging Liquid Jet Reactor (CPLJR) as an aeration and brine dispenser technique for the environmental safe discharge of brine from Kuwaits desalination plants, in: 2Nd Int. Conf. Power Energy Eng., Munich, Germany, 2017.
- [34] P.J.W. Roberts, A. Ferrier, G. Daviero, Mixing in inclined dense jets, J. Hydraul. Eng. 123 (1997) 693–699, [https://doi.org/10.1061/\(asce\)0733-9429\(1997\)123:8\(693\)](https://doi.org/10.1061/(asce)0733-9429(1997)123:8(693)).
- [35] G.A. Kikkert, M.J. Davidson, R.I. Nokes, Inclined negatively buoyant discharges, J. Hydraul. Eng. 133 (2007) 545–554, [https://doi.org/10.1061/\(asce\)0733-9429\(2007\)133:5\(545\)](https://doi.org/10.1061/(asce)0733-9429(2007)133:5(545)).
- [36] D. Shao, A.W.K. Law, Mixing and boundary interactions of 30° and 45° inclined dense jets, Environ. Fluid Mech. 10 (2010) 521–553, <https://doi.org/10.1007/s10652-010-9171-2>.
- [37] I.G. Papakonstantis, G.C. Christodoulou, P.N. Papanicolaou, Inclined negatively buoyant jets 2: concentration measurements, J. Hydraul. Res. 49 (2011) 13–22, <https://doi.org/10.1080/00221686.2010.542617>.
- [38] C.J. Oliver, M.J. Davidson, R.I. Nokes, Behavior of dense discharges beyond the return point, J. Hydraul. Eng. 139 (2013) 1304–1308, [https://doi.org/10.1061/\(asce\)hy.1943-7900.0000781](https://doi.org/10.1061/(asce)hy.1943-7900.0000781).
- [39] O. Abessi, P.J.W. Roberts, Effect of nozzle orientation on dense jets in stagnant environments, J. Hydraul. Eng. 141 (2015), [https://doi.org/10.1061/\(asce\)hy.1943-7900.0001032](https://doi.org/10.1061/(asce)hy.1943-7900.0001032).
- [40] B.S. Al-Anzi, Performance of a Novel Confined Plunging Jet Reactor Incorporating an Annular Airlift Column, Loughborough University, 2007.
- [41] B.S. Al-Anzi, Effect of primary variables on a confined plunging liquid jet reactor, Water (Switzerland), 12 (2020). doi:<https://doi.org/10.3390/w12030764>.
- [42] A. Boualouache, F. Zidouni Kendil, A. Mataoui, Numerical assessment of two phase flow modeling using plunging jet configurations, Chem. Eng. Res. Des. 128 (2017) 248–256, <https://doi.org/10.1016/j.cherd.2017.10.024>.
- [43] X.L. Qu, L. Khezzar, D. Danciu, M. Labois, D. Lakehal, Characterization of plunging liquid jets: a combined experimental and numerical investigation, Int. J. Multiph. Flow. 37 (2011) 722–731, <https://doi.org/10.1016/j.ijmultiphaseflow.2011.02.006>.
- [44] T. Fonty, M. Ferrand, A. Leroy, D. Violeau, Air entrainment modeling in the SPH method: a two-phase mixture formulation with open boundaries, flow, Turbul. Combust. 105 (2020) 1149–1195, <https://doi.org/10.1007/s10494-020-00165-7>.
- [45] V.E. Badalassi, H.D. Ceniceros, S. Banerjee, Computation of multiphase systems with phase field models, J. Comput. Phys. 190 (2003) 371–397, [https://doi.org/10.1016/S0021-9991\(03\)00280-8](https://doi.org/10.1016/S0021-9991(03)00280-8).
- [46] J. Kim, S. Lee, Y. Choi, S.M. Lee, D. Jeong, Basic principles and practical applications of the Cahn-Hilliard equation, Math. Probl. Eng. 2016 (2016), <https://doi.org/10.1155/2016/9532608>.
- [47] C.T. Hsiao, X. Wu, J. Ma, G.L. Chahine, Numerical and experimental study of bubble entrainment due to a horizontal plunging jet, in: Int. Shipbuild. Prog., 2013: pp. 435–469. doi:<https://doi.org/10.3233/ISP-130093>.
- [48] A. Boualouache, F. Zidouni, A. Mataoui, Numerical visualization of plunging water jet using volume of fluid model, J. Appl. Fluid Mech. 11 (2018) 95–105. doi:[10.29252/jafm.11.01.27861](https://doi.org/10.29252/jafm.11.01.27861).
- [49] Z. Yin, Q. Jia, Y. Li, Y. Wang, D. Yang, Computational study of a vertical plunging jet into stillwater, Water (Switzerland). 10 (2018). doi:<https://doi.org/10.3390/w10080989>.
- [50] D. Lucas, E. Krepper, H.M. Prasser, Use of models for lift, wall and turbulent dispersion forces acting on bubbles for poly-disperse flows, Chem. Eng. Sci. 62 (2007) 4146–4157, <https://doi.org/10.1016/j.ces.2007.04.035>.
- [51] E. Jones, M. Qadir, M.T.H. van Vliet, V. Smakhtin, S. mu Kang, The state of desalination and brine production: a global outlook, Sci. Total Environ. 657 (2019) 1343–1356. doi:<https://doi.org/10.1016/j.scitotenv.2018.12.076>.
- [52] B.R. Hodges, J.E. Furnans, P.S. Kulis, Thin-layer gravity current with implications for desalination brine disposal, J. Hydraul. Eng. 137 (2011) 356–371, [https://doi.org/10.1061/\(asce\)hy.1943-7900.0000310](https://doi.org/10.1061/(asce)hy.1943-7900.0000310).
- [53] E.E. Adams, I. Shrivastava, A.C. Chow, Vertical mixing of desalination reject brine that accumulates in local depressions after near field mixing, Am. Geophys. Union (2016) pp. HI34B-1813, <https://ui.adsabs.harvard.edu/abs/2016AGUOSH134B1813C>.
- [54] J.M. Miller, A comparison of fish kills in the Pamlico River and the Neuse River in Coastal North Carolina (a symptom) and abiotic factors (the root causes), Oceanogr. Fish. Open Access J. 7 (2018), <https://doi.org/10.19080/ofoaj.2018.07.555701>.
- [55] J.A. Nestlerode, R.E. Diaz, Effects of periodic environmental hypoxia on predation of a tethered polychaete, Glycera americana: implications for trophic dynamics, Mar. Ecol. Prog. Ser. 172 (1998) 185–195, <https://doi.org/10.3354/meps172185>.
- [56] J. Lin, L. Xie, L.J. Pietrafesa, J. Shen, M.A. Mallin, M.J. Durako, Dissolved oxygen stratification in two micro-tidal partially-mixed estuaries, Estuar. Coast. Shelf Sci. 70 (2006) 423–437, <https://doi.org/10.1016/j.ecss.2006.06.032>.
- [57] C. Yang, Z.S. Mao, Numerical simulation of interphase mass transfer with the level set approach, Chem. Eng. Sci. 60 (2005) 2643–2660, <https://doi.org/10.1016/j.ces.2004.11.054>.
- [58] M. Wörner, Numerical modeling of multiphase flows in microfluidics and micro process engineering: a review of methods and applications, Microfluid. Nanofluid. 12 (2012) 841–886, <https://doi.org/10.1007/s10404-012-0940-8>.
- [59] M.T. Flavin, D.K. Freeman, J. Han, Interfacial ion transfer and current limiting in neutral-carrier ion-selective membranes: a detailed numerical model, J. Membr. Sci. 572 (2019) 374–381, <https://doi.org/10.1016/j.memsci.2018.10.065>.
- [60] J. Yoon, M.T. Flavin, J. Han, Current efficiency and selectivity reduction caused by co-ion leakage in electromembrane processes, Water Res. (2021), <https://doi.org/10.1016/j.watres.2021.117351>.
- [61] M.T. Flavin, C.A. Lissandrello, J. Han, Real-time, dynamic monitoring of selectively driven ion-concentration polarization, Electrochim. Acta (2022), <https://doi.org/10.1016/j.electacta.2022.140770>.
- [62] D. Lakehal, M. Meier, F. Fulgosí, Interface tracking towards the direct simulation of heat and mass transfer in multiphase flows, Int. J. Heat Fluid Flow 23 (2002) 242–257, [https://doi.org/10.1016/S0142-727X\(02\)00172-8](https://doi.org/10.1016/S0142-727X(02)00172-8).
- [63] C.W. Hirt, B.D. Nichols, Volume of fluid (VOF) method for the dynamics of free boundaries, J. Comput. Phys. 39 (1981) 201–225, [https://doi.org/10.1016/0021-9991\(81\)90145-5](https://doi.org/10.1016/0021-9991(81)90145-5).
- [64] B.E. Launder, D.B. Spalding, The numerical computation of turbulent flows, Comput. Methods Appl. Mech. Eng. 3 (1974) 269–289, [https://doi.org/10.1016/0045-7825\(74\)90029-2](https://doi.org/10.1016/0045-7825(74)90029-2).
- [65] A.J. Bard, L.R. Faulkner, Electrochemical Methods: Fundamentals and Applications, Wiley, 2000. <https://books.google.com/books?id=kv56QgAACAAJ>.
- [66] A. Ohkawa, D. Kusabiraki, Y. Kawai, N. Sakai, K. Endoh, Some flow characteristics of a vertical liquid jet system having downcomers, Chem. Eng. Sci. 41 (1986) 2347–2361, [https://doi.org/10.1016/0009-2509\(86\)85085-0](https://doi.org/10.1016/0009-2509(86)85085-0).
- [67] B.S. Al-Anzi, I.W. Cumming, C.D. Rielly, Air entrainment rates in a confined plunging jet reactor, in: 10th Int. Conf. Multiph. Flow Ind. Plants, Italy, 2006, pp. 71–82.
- [68] K.T. Kiger, J.H. Duncan, Air-entrainment mechanisms in plunging jets and breaking waves, Annu. Rev. Fluid Mech. 44 (2011) 563–596, <https://doi.org/10.1146/annurev-fluid-122109-160724>.
- [69] C. Amatore, S. Szunerits, L. Thouin, J.S. Warkocz, The real meaning of Nernst's steady diffusion layer concept under non-forced hydrodynamic conditions. A simple model based on Levich's seminal view of convection, J. Electroanal. Chem. 500 (2001) 62–70, [https://doi.org/10.1016/S0022-0728\(00\)00378-8](https://doi.org/10.1016/S0022-0728(00)00378-8).